Available online at www.sciencedirect.com
SCIENCE DIRECT®
International Journal of Heat and Mass Transfer 47 (2004) 2251–2259
International Journal of HEAT and MASS TRANSFER
www.elsevier.com/locate/ijhmt

# Rayleigh–Bénard convection of viscoelastic fluids in arbitrary finite domains

H.M. Park *, K.S. Park

*Department of Chemical Engineering, Sogang University, P.O. Box 1142, Shinsoo-Dong Mapo-Gu, Seoul 100611, South Korea*

Received 12 August 2003; received in revised form 15 November 2003

**Abstract**

In the present work, we consider the linear hydrodynamic stability problems of viscoelastic fluids in arbitrary finite domains. The effects of domain shapes on the critical Rayleigh number and convection pattern are investigated by means of a linear stability analysis employing a Chebyshev pseudospectral method. It is shown that the domain shape can change the viscoelastic parameter values where the Hopf bifurcation occurs in the Rayleigh–Bénard convection. The results of the present investigation may be exploited to design shapes of convection box where the Hopf bifurcation occurs at realistic low values of Deborah number. This will enhance the usefulness of the natural convection system as a rheometry tool.


*Keywords:* Rayleigh–Bènard convection; Arbitrary finite domains; Viscoelastic fluids

## 1. Introduction

In our previous works [1–3], we have investigated the Rayleigh–Bénard convection problems of viscoelastic fluids in finite rectangular domains with no-slip sidewalls. With the help of a Chebyshev pseudospectral method, the effects of box aspect ratio and various rheological parameters on the critical Rayleigh number and convection cell size have been studied and, furthermore, the natural convection system is suggested as a new practical tool of rheometry. In the present work, we study the Rayleigh–Bénard convection of viscoelastic fluids in arbitrary shaped domains. Our purpose is to investigate how the shape of the domain changes the critical Rayleigh number and the bifurcation sequences. Special interest is in the shape where the Hopf bifurcation occurs at a lower values of Deborah number. When we want to adopt the natural convection system as a tool of rheometry, it is more useful to invoke various phenomena peculiar to the viscoelasticity in the convection box. But it is shown that the Hopf bifurcation in the Rayleigh–Bénard convection of viscoelastic fluids in the horizontally unbounded domain occurs at unrealistically high values of Deborah number[4]. Thus, if a specific shape of the convection box induces the Hopf bifurcation at a lower Deborah number, that shaped box may be considered as a better equipment to estimate the rheological parameter values of a specific viscoelastic fluid.

Until now, there have been no appropriate analysis tools for this interesting problems of hydrodynamic stability in arbitrary shaped domains. But recently we proposed a method of linear and nonlinear hydrodynamic stability analysis in confined rectangular domains with no-slip walls [1–3] by exploiting the Chebyshev pseudospectral method [5]. In the present investigation, we employ the same Chebyshev pseudospectral method to solve the linear Rayleigh–Bénard convection problems in two-dimensional arbitrary finite domains. After transforming the arbitrary shaped physical domains to a square computational domain, we reformulate the Boussinesq equation using the stream function so that the incompressibility condition is imposed exactly. The discretization through the Chebyshev pseudospectral

* Corresponding author. Tel.: +82-7058-482; fax: +82-7110-439.
*E-mail address:* hmpark@ccs.sogang.ac.kr (H.M. Park).

0017-9310/$ - see front matter © 2003 Elsevier Ltd. All rights reserved.
doi:10.1016/j.ijheatmasstransfer.2003.11.022

**Nomenclature**

| | |
|---|---|
| $a$ | rheological parameter defined in Eq. (4) |
| $d_x$ | half width of the domain |
| $d_y$ | half depth of the domain |
| $\mathscr{D}$ | Jaumann differential operator defined in Eq. (10) |
| $g_r$ | gravitational constant |
| $\sqrt{g}$ | Jacobian of domain transformation |
| $\mathbf{g}^i$ | the $i$th contravariant basis vector (Eq. (35)) |
| $g^{ij}$ | contravariant metric tensor |
| $k$ | thermal conductivity |
| $P$ | pressure |
| $Pr$ | Prandtl number |
| $R$ | Rayleigh number |
| $S$ | difference of normal stresses (Eq. (25)) |
| $T$ | temperature |
| $U$ | sum of normal stresses (Eq. (26)) |
| $\mathbf{v}$ | velocity |

*Greek symbols*

| | |
|---|---|
| $\alpha$ | thermal expansion coefficient |
| $\Gamma$ | time derivative of the stream function |
| $\dot{\boldsymbol{\gamma}}$ | rate of deformation tensor |
| $\epsilon$ | rheological parameter defined in Eq. (4) |
| $\kappa$ | rheological parameter defined in Eq. (4) |
| $\lambda$ | Deborah number |
| $\mu_0$ | viscosity |
| $\boldsymbol{\tau}$ | stress tensor |
| $\Psi$ | stream function |
| $\boldsymbol{\omega}$ | spin tensor |

method yields algebraic eigenvalue problems which can be solved to find the eigenvalues and eigenvectors needed in the linear stability analysis. A very general constitutive equation is employed in the present work that encompasses the Maxwell model, Oldroyd model and Phan–Thien–Tanner model. The effects of the shape of the domain and rheological parameter values on the critical Rayleigh number and convection pattern are examined.

## 2. Governing equations

We consider a Boussinesq fluid in a two-dimensional arbitrary finite domain whose bottom is maintained at a higher temperature than the top. The shapes of the domain are such that the top and bottom are flat, whereas the sidewalls are of arbitrary shapes. Governing equations in dimensionless variables may be written as:

$$\nabla \cdot \mathbf{v} = 0, \tag{1}$$

$$\frac{\partial \mathbf{v}}{\partial t} + \mathbf{v} \cdot \nabla \mathbf{v} = -Pr\nabla P + Pr\nabla \cdot \boldsymbol{\tau} + RPrT\mathbf{j}, \tag{2}$$

$$\frac{\partial T}{\partial t} + \mathbf{v} \cdot \nabla T = \nabla^2 T, \tag{3}$$

$$\boldsymbol{\tau} + \lambda\left\{\kappa(tr\boldsymbol{\tau})\boldsymbol{\tau} + \mathscr{D}\boldsymbol{\tau} - \frac{1}{2}a(\boldsymbol{\tau}\cdot\dot{\boldsymbol{\gamma}} + \dot{\boldsymbol{\gamma}}\cdot\boldsymbol{\tau})\right\} = \dot{\boldsymbol{\gamma}} + \epsilon\lambda\left\{\mathscr{D}\dot{\boldsymbol{\gamma}} - a\dot{\boldsymbol{\gamma}}\cdot\dot{\boldsymbol{\gamma}}\right\}. \tag{4}$$

In the above equations, the dimensionless variables have been defined by the following equations, where the superscript asterisk is used to denote the dimensional quantities.

$$x = \frac{x^*}{d_y}, \quad y = \frac{y^*}{d_y}, \quad t = \frac{\kappa t^*}{d_y^2}, \quad \mathbf{v} = \frac{d_y \mathbf{v}^*}{\kappa},$$

$$T = \frac{T^* - T^*_{\text{cold}}}{T^*_{\text{hot}} - T^*_{\text{cold}}}, \quad P' = \frac{d_y^2 p^*}{\mu_0 \kappa}, \quad \boldsymbol{\tau} = \frac{d_y \boldsymbol{\tau}^*}{\mu_0 k}, \tag{5}$$

where $T^*$ is the dimensional temperature field, $T^*_{\text{cold}}$ the temperature at the top boundary, $T^*_{\text{hot}}$ the temperature at the bottom boundary, $t^*$ the time, $\mathbf{v}^*$ the velocity field, $P^*$ the pressure field, $\boldsymbol{\tau}^*$ the stress tensor, $\kappa$ the thermal diffusivity, $\rho$ the density, $\mu_0$ the viscosity, $d_y$ the characteristic depth of the domain. In Eq. (2), $P$ is the modified pressure given by

$$P = P' - \frac{(T^*_{\text{cold}} - T^*_{\text{hot}})}{2}\frac{\rho_0 d_y^3}{k\mu_0}\alpha g_r y \tag{6}$$

and $\alpha$ is the thermal expansion coefficient. The dimensionless group $R$ is the Rayleigh number and $Pr$ is the Prandtl number defined as follows:

$$Ra = \alpha g_r \frac{(T^*_{\text{hot}} - T^*_{\text{cold}})d_y^3 \rho_0}{\kappa\mu_0}, \tag{7}$$

$$Pr = \frac{\mu_0}{\kappa\rho_0}. \tag{8}$$

In Eq. (4), $\lambda$ is the Deborah number defined by

$$\lambda = \frac{k\lambda^*}{d_y^2}, \tag{9}$$

where $\lambda^*$ is the stress relaxation time. The Jaumann differential operator is defined as

$$\mathscr{D} \equiv \frac{\partial}{\partial t} + \mathbf{v}\cdot\nabla + \frac{1}{2}(\boldsymbol{\omega}\cdot - - \cdot\boldsymbol{\omega}), \tag{10}$$

where the spin tensor $\boldsymbol{\omega}$ is given by

$$\boldsymbol{\omega} \equiv \nabla \mathbf{v} - (\nabla \mathbf{v})^{\mathrm{T}} \tag{11}$$

and rate of deformation tensor $\dot{\boldsymbol{\gamma}}$ is

$$\dot{\boldsymbol{\gamma}} = \nabla \mathbf{v} + (\nabla \mathbf{v})^{\mathrm{T}}. \tag{12}$$

With an appropriate isothermal sidewalls, there exists a critical Rayleigh number for the domains under consideration below which there is no fluid motion. The basic state or the conduction state $(\mathbf{v}^{\mathrm{s}}, T^{\mathrm{s}})$ that prevails in the system below the critical Rayleigh number is given by;

$$\mathbf{v}^{\mathrm{s}} = 0, \tag{13}$$

$$\nabla^2 T^{\mathrm{s}} = 0. \tag{14}$$

The relevant boundary conditions are; no velocity slip on all bounding walls, $T^{\mathrm{s}} = 1.0$ at the bottom, $T^{\mathrm{s}} = 0.0$ at the top boundary and Dirichlet temperature boundary condition on the sidewalls, where temperature decreases linearly with respect to the height. If we define the deviational temperature $\Theta$ by

$$\Theta = T - T^{\mathrm{s}}. \tag{15}$$

Eqs. (1)–(3) may be rewritten as;

$$\nabla \cdot \mathbf{v} = 0, \tag{16}$$

$$\frac{\partial \mathbf{v}}{\partial t} + \mathbf{v} \cdot \nabla \mathbf{v} = -Pr \nabla P + Pr \nabla \cdot \boldsymbol{\tau} + RPr \Theta \mathbf{j}, \tag{17}$$

$$\frac{\partial \Theta}{\partial t} + \mathbf{v} \cdot \nabla \Theta + \mathbf{v} \cdot \nabla T^{\mathrm{s}} = \nabla^2 \Theta. \tag{18}$$

The relevant boundary conditions are; $\mathbf{v} = 0$ and $\Theta = 0$ on all bounding walls. The stream function $\Psi$ is employed instead of $\mathbf{v}$ and $P$ to analyze flows in two-dimensional domains. In terms of the stream function, (4) and (16)–(18) may be rewritten after deleting nonlinear terms [1]:

$$\frac{\partial}{\partial t} \nabla^2 \Psi + RPr \frac{\partial \Theta}{\partial x} - Pr \frac{\partial^2 S}{\partial x \partial y} - Pr \Delta \tau_{xy} = 0, \tag{19}$$

$$\frac{\partial \Theta}{\partial t} - \frac{\partial T^{\mathrm{s}}}{\partial y} \frac{\partial \Psi}{\partial x} + \frac{\partial T^{\mathrm{s}}}{\partial x} \frac{\partial \Psi}{\partial y} - \nabla^2 \Theta = 0, \tag{20}$$

$$\tau_{xy} + \lambda \frac{\tau_{xy}}{\partial t} = \Delta \Psi + \epsilon \lambda \frac{\partial}{\partial t} \Delta \Psi, \tag{21}$$

$$S + \lambda \frac{\partial S}{\partial t} = 4 \frac{\partial^2 \Psi}{\partial x \partial y} + 4 \epsilon \lambda \frac{\partial}{\partial t} \frac{\partial^2 \Psi}{\partial x \partial y}, \tag{22}$$

$$U + \lambda \frac{\partial U}{\partial t} = 0, \tag{23}$$

where

$$\Delta \equiv \frac{\partial^2}{\partial y^2} - \frac{\partial^2}{\partial x^2}, \tag{24}$$

$$S \equiv \tau_{xx} - \tau_{yy}, \tag{25}$$

$$U \equiv \tau_{xx} + \tau_{yy}. \tag{26}$$

The boundary conditions are such that the stream function $\Psi$ and its normal derivative, $\Psi$ and $\frac{\partial \Psi}{\partial n}$, and $\Theta$ are zero at the walls. In (20), $\frac{\partial T^{\mathrm{s}}}{\partial x} = 0$ if $T^{\mathrm{s}}$ is determined with the isothermal sidewalls whose temperature decreases linearly with respect to the height for the domains where the top and bottom boundaries are flat. Removing $S$ and $\tau_{xy}$ in (19) in favor of $\Psi$ by exploiting (21) and (22), Eq. (19) becomes

$$\begin{aligned} &\left(1 + \lambda \frac{\partial}{\partial t}\right) \nabla^2 \frac{\partial \Psi}{\partial t} + RPr \frac{\partial}{\partial x} \left(1 + \lambda \frac{\partial}{\partial t}\right) \Theta \\ &\quad - Pr \frac{\partial^2}{\partial x \partial y} 4 \left(1 + \epsilon \lambda \frac{\partial}{\partial t}\right) \frac{\partial^2 \Psi}{\partial x \partial y} \\ &\quad - Pr \Delta \left(1 + \epsilon \lambda \frac{\partial}{\partial t}\right) \Delta \Psi = 0. \end{aligned} \tag{27}$$

Finally, the governing equations for the linear stability analysis may be rearranged in the following form:

$$\frac{\partial \Psi}{\partial t} = \Gamma, \tag{28}$$

$$\begin{aligned} \lambda \frac{\partial}{\partial t} \nabla^2 \Gamma + RPr \lambda \frac{\partial}{\partial t} \frac{\partial \Theta}{\partial x} &= Pr \nabla^4 \Psi + Pr \epsilon \lambda \nabla^4 \Gamma \\ &\quad - \nabla^2 \Gamma - RPr \frac{\partial \Theta}{\partial x}, \end{aligned} \tag{29}$$

$$\frac{\partial \Theta}{\partial t} = \frac{\partial T^{\mathrm{s}}}{\partial y} \frac{\partial \Psi}{\partial x} - \frac{\partial T^{\mathrm{s}}}{\partial x} \frac{\partial \Psi}{\partial y} + \nabla^2 \Theta. \tag{30}$$

The boundary condition for $\Gamma$ are the same as those for $\Psi$, since the boundary conditions are time-independent.

Now, we transform the arbitrary shaped physical domain $(x, y)$ to a fixed square computational domain $(\xi, \eta)$. Then the governing equations (28)–(30) may be rewritten in the computational domain as;

$$\frac{\partial \Psi}{\partial t} = \Gamma, \tag{31}$$

$$\begin{aligned} &\lambda \frac{\partial}{\partial t} \left\{ \frac{1}{\sqrt{g}} \frac{\partial}{\partial \xi^i} \left( \sqrt{g} g^{ij} \frac{\partial}{\partial \xi^j} \right) \right\} \Gamma + RPr \lambda \frac{\partial}{\partial t} \left\{ \epsilon_{ij3} \frac{1}{\sqrt{g}} \frac{\partial \Theta}{\partial \xi^l} y_{\xi^j} \right\} \\ &\quad = Pr \frac{1}{\sqrt{g}} \frac{\partial}{\partial \xi^i} \left[ \sqrt{g} g^{ij} \frac{\partial}{\partial \xi^j} \left\{ \frac{1}{\sqrt{g}} \frac{\partial}{\partial \xi^k} \left( \sqrt{g} g^{kl} \frac{\partial \Psi}{\partial \xi^l} \right) \right\} \right] \\ &\qquad + Pr \epsilon \lambda \frac{1}{\sqrt{g}} \frac{\partial}{\partial \xi^i} \left[ \sqrt{g} g^{ij} \frac{\partial}{\partial \xi^j} \left\{ \frac{1}{\sqrt{g}} \frac{\partial}{\partial \xi^k} \left( \sqrt{g} g^{kl} \frac{\partial \Gamma}{\partial \xi^l} \right) \right\} \right] \\ &\qquad - \frac{1}{\sqrt{g}} \frac{\partial}{\partial \xi^i} \left( \sqrt{g} g^{ij} \frac{\partial \Gamma}{\partial \xi^j} \right) - RPr \epsilon_{ij3} \frac{1}{\sqrt{g}} \frac{\partial \Theta}{\partial \xi^i} y_{\xi^j}, \end{aligned} \tag{32}$$

$$\begin{aligned} \frac{\partial \Theta}{\partial t} &= \left( \epsilon_{ij3} \frac{1}{\sqrt{g}} \frac{\partial \Psi}{\partial \xi^i} y_{\xi^j} \right) \left( \epsilon_{kl3} \frac{1}{\sqrt{g}} \frac{\partial T^{\mathrm{s}}}{\partial \xi^l} x_{\xi^k} \right) \\ &\quad - \left( \epsilon_{ij3} \frac{1}{\sqrt{g}} \frac{\partial \Psi}{\partial \xi^j} x_{\xi^i} \right) \left( \epsilon_{kl3} \frac{1}{\sqrt{g}} \frac{\partial T^{\mathrm{s}}}{\partial \xi^k} y_{\xi^l} \right) \\ &\quad + \frac{1}{\sqrt{g}} \frac{\partial}{\partial \xi^i} \left( \sqrt{g} g^{ij} \frac{\partial \Theta}{\partial \xi^j} \right), \end{aligned} \tag{33}$$

where

$$\sqrt{g} = \frac{\partial x}{\partial \xi}\frac{\partial y}{\partial \eta} - \frac{\partial y}{\partial \xi}\frac{\partial x}{\partial \eta}, \tag{34}$$

$$\mathbf{g}^1 = \frac{1}{\sqrt{g}}\left(\mathbf{i}\frac{\partial y}{\partial \eta} - \mathbf{j}\frac{\partial x}{\partial \eta}\right), \tag{35}$$

$$\mathbf{g}^2 = \frac{1}{\sqrt{g}}\left(-\mathbf{i}\frac{\partial y}{\partial \xi} + \mathbf{j}\frac{\partial x}{\partial \xi}\right), \tag{36}$$

$$g^{ij} = \mathbf{g}^i \cdot \mathbf{g}^j. \tag{37}$$

Repeated indices imply summation over 1 and 2, $x_{\xi^i} \equiv \frac{\partial x}{\partial \xi^i}$, $y_{\xi^i} \equiv \frac{\partial y}{\partial \xi^i}$ and $\xi^1 = \xi$, $\xi^2 = \eta$. The transformation between the physical domain $(x, y)$ and the computational domain $(\xi, \eta)$ is performed by means of the following set of elliptic equations [6].

$$(\sqrt{g})^2 g^{11}\frac{\partial^2 x}{\partial \xi^2} + 2(\sqrt{g})^2 g^{12}\frac{\partial^2 x}{\partial \xi \partial \eta} + (\sqrt{g})^2 g^{22}\frac{\partial^2 x}{\partial \eta^2} = -(\sqrt{g})^2\left(P\frac{\partial x}{\partial \xi} + Q\frac{\partial x}{\partial \eta}\right), \tag{38}$$

$$(\sqrt{g})^2 g^{11}\frac{\partial^2 y}{\partial \xi^2} + 2(\sqrt{g})^2 g^{12}\frac{\partial^2 y}{\partial \xi \partial \eta} + (\sqrt{g})^2 g^{22}\frac{\partial^2 y}{\partial \eta^2} = -(\sqrt{g})^2\left(P\frac{\partial y}{\partial \xi} + Q\frac{\partial y}{\partial \eta}\right). \tag{39}$$

The variables $P$ and $Q$ in (38) and (39) are adjusted such that the grids intersect the boundary orthogonally. As a result the boundary conditions for (31)–(33) are given by:

$$\xi = \pm 1;\ \Psi = 0,\quad \frac{\partial \Psi}{\partial \xi} = 0,\quad \Gamma = 0,\quad \frac{\partial \Gamma}{\partial \xi} = 0,\quad \Theta = 0, \tag{40}$$

$$\eta = \pm 1;\ \Psi = 0,\quad \frac{\partial \Psi}{\partial \eta} = 0,\quad \Gamma = 0,\quad \frac{\partial \Gamma}{\partial \eta} = 0,\quad \Theta = 0. \tag{41}$$

## 3. Linear stability analysis

Assuming

$$\Psi(\xi, \eta) = e^{st}\varphi(\xi, \eta), \tag{42}$$

$$\Gamma(\xi, \eta) = e^{st}\gamma(\xi, \eta), \tag{43}$$

$$\Theta(\xi, \eta) = e^{st}\theta(\xi, \eta). \tag{44}$$

Eqs. (31)–(33) become a differential eigenvalue problem, where $s$ is the eigenvalue determining the stability of the basic state. The boundary conditions for $\varphi$, $\gamma$ and $\theta$ are the same as those for $\Psi$, $\Gamma$ and $\Theta$, respectively. As previously [1–3], the Chebyshev pseudospectral method [5] is employed to convert the differential eigenvalue problem to an algebraic eigenvalue problem after imposing relevant boundary conditions. Using the Chebyshev pseudospectral method, we can approximate differentiations of a function by matrix multiplications as follows:

$$\frac{\partial^q f}{\partial x^q}(x_i, y_j) = \sum_{l=1}^{NX+1} \widehat{GX}_{i,l}^{(q)} f_{l,j}, \tag{45}$$

$$\frac{\partial^q f}{\partial y^q}(x_i, y_j) = \sum_{l=1}^{NY+1} \widehat{GY}_{j,l}^{(q)} f_{i,l} \quad (1 \leqslant i \leqslant NX+1,\ 1 \leqslant j \leqslant NY+1), \tag{46}$$

where $(x_i, y_j)$ is the Chebyshev collocation point [1], the grid variable $f_{l,j}$ is the value of $f(\xi, \eta)$ at the collocation point $(\xi_l, \eta_j)$, $NX+1$ is the total number of grids in the $\xi$ direction, $NY+1$ is that in the $\eta$ direction. The matrices $\widehat{GX}_{i,l}^{(q)}$ and $\widehat{GY}_{j,l}^{(q)}$ have been derived in reference [1]. For the variables $\varphi$ and $\gamma$, we impose two separate boundary conditions on each boundary wall. Therefore, we can remove the boundary grid values and the outermost internal grid values of $\varphi$ in terms of the remaining internal grid values. For example, the boundary conditions (40) for $\varphi$ yields [1]:

$$\varphi_{1,j} = 0;\ \varphi_{NX+1,j} = 0 \quad (1 \leqslant j \leqslant NY+1), \tag{47}$$

$$\sum_{m=1}^{NX+1} \widehat{GX}_{1,m}^{(1)}\varphi_{m,j} = 0;\ \sum_{m=1}^{NX+1} \widehat{GX}_{NX+1,m}^{(1)}\varphi_{m,j} = 0 \quad (1 \leqslant j \leqslant NY+1). \tag{48}$$

Solving Eqs. (47) and (48) simultaneously, we can express the outermost internal grid values in terms of the remaining internal grid values [1];

$$\varphi_{2,j} = \sum_{m=3}^{NX-1} a_m \varphi_{m,j};$$

$$\varphi_{NX,j} = \sum_{m=3}^{NX-1} b_m \varphi_{m,j} \quad (1 \leqslant j \leqslant NY+1), \tag{49}$$

where

$$a_m \equiv \frac{\widehat{GX}_{1,NX}^{(1)}\widehat{GX}_{NX+1,m}^{(1)} - \widehat{GX}_{NX+1,NX}^{(1)}\widehat{GX}_{1,m}^{(1)}}{\widehat{GX}_{1,2}^{(1)}\widehat{GX}_{NX+1,NX}^{(1)} - \widehat{GX}_{1,NX}^{(1)}\widehat{GX}_{NX+1,2}^{(1)}}, \tag{50}$$

$$b_m \equiv \frac{\widehat{GX}_{NX+1,2}^{(1)}\widehat{GX}_{1,m}^{(1)} - \widehat{GX}_{1,2}^{(1)}\widehat{GX}_{NX+1,m}^{(1)}}{\widehat{GX}_{1,2}^{(1)}\widehat{GX}_{NX+1,NX}^{(1)} - \widehat{GX}_{1,NX}^{(1)}\widehat{GX}_{NX+1,2}^{(1)}}. \tag{51}$$

In a similar manner, the outermost internal grid values $\varphi_{i,2}$ and $\varphi_{i,NY}$ can be represented in terms of the remaining internal grid values [1]. Therefore, the unknown grid values to be determined in the resulting algebraic eigenvalue problem are

$$\mathbf{x} = (\varphi_{3,3}, \varphi_{4,3}, \ldots, \varphi_{NX-1,NY-1}, \gamma_{3,3}, \gamma_{4,3}, \ldots, \gamma_{NX-1,NY-1}, \theta_{2,2}, \theta_{3,2}, \ldots, \theta_{NX,NY})^{\mathrm{T}}. \tag{52}$$

The resulting algebraic eigenvalue problem may be written as

$$\boldsymbol{\alpha} \cdot \mathbf{x} = s\boldsymbol{\beta} \cdot \mathbf{x}, \tag{53}$$

where the matrices $\boldsymbol{\alpha}$ and $\boldsymbol{\beta}$ are constructed by discretizing Eqs. (31)–(33) after substituting Eqs. (42)–(44). The basic state becomes unstable and convective flow sets in when the real part of $s$ becomes positive. The critical Rayleigh number is defined as the smallest Rayleigh number when the largest real part of $s$ is zero. For Rayleigh–Bénard convection of Newtonian fluids, when the largest real part of $s$ is zero, the corresponding imaginary part of $s$ is always zero; i.e., the exchange of stabilities is valid [7]. On the other hand, the imaginary part of $s$ may be nonzero at the neutrally stable state for the Rayleigh–Bénard convection of viscoelastic fluids, depending on the values of $\lambda$ and $\epsilon$ in the constitutive equations [1–3]. This phenomenon, called the overstability or Hopf bifurcation, is peculiar to the viscoelastic fluids and may be exploited to characterize the viscoelastic fluids. It shall be shown in the sequel that the shape of domain also affects the occurrence of the Hopf bifurcation. The matrix eigenvalue problem (53) is solved by using a standard package such as IMSL. We adopt a $(30\times15)$ grids with double precision arithmetic. Employment of a finer grid system $(40\times20)$ does not change the results significantly.

## 4. Results

Fig. 1 shows the critical Rayleigh number and the boundary separating the region of exchange of stabilities and that of Hopf bifurcation for the case of isothermal sidewalls in the $\epsilon$–$\lambda$ plane for a rectangular domain with the aspect ratio $d_x/d_y = 2.0$, where $d_x$ is the width and $d_y$ is the depth of the domain. In our previous work [1], we adopt the half depth of the domain as the characteristic length when converting the governing equations to the dimensionless form. In the present investigation, however, we adopt the depth of the domain as the characteristic length. Therefore the *Ra* in the present work is eight times as large as that in reference [1], while $\lambda$ in the present work is one fourth of that in reference [1]. From Fig. 1, we find that the critical Rayleigh number *Rc* remains the same regardless of $(\epsilon, \lambda)$ values when the exchange of stabilities is valid. This value is actually the critical Rayleigh number for the Newtonian fluids [1]. As $\epsilon$ decreases or $\lambda$ increases, the overstability occurs, and *Rc* decreases rapidly as $\epsilon$ decreases or $\lambda$ increases. The Deborah number $\lambda$ indicates the elasticity of the fluid, which is an important mechanism that induces overstability. Fig. 2 shows the critical Rayleigh number for the aspect ratio in the range 1–4, when $\lambda = 0.0$ (Newtonian

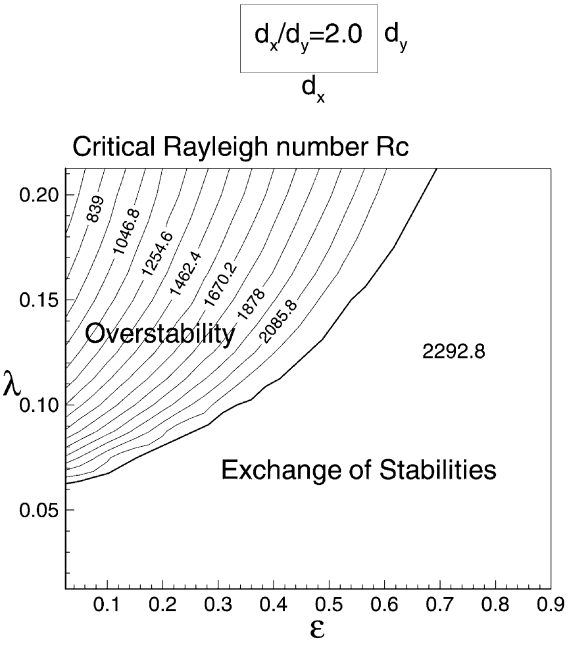


Fig. 1. The critical Rayleigh number and the boundary separating exchange of stabilities and Hopf bifurcation in the $\epsilon$–$\lambda$ plane for the rectangular domain of $d_x/d_y = 2.0$.

fluids), $(\epsilon, \lambda) = (0.6, 0.0075)$ and $(\epsilon, \lambda) = (0.2, 0.1)$, for the case of adiabatic sidewalls ($\frac{\partial \Theta}{\partial x} = 0$) and isothermal sidewalls ($\Theta = 0$), respectively. From Ref. [1] (adiabatic sidewalls) and Fig. 1 of the present work (isothermal sidewalls), we find that the exchange of stabilities is valid for the case $(\epsilon, \lambda) = (0.6, 0.0075)$, while Hopf bifurcation occurs for $(\epsilon, \lambda) = (0.2, 0.1)$ when $d_x/d_y = 2.0$ for both thermal boundary conditions. The adiabatic case has been extensively investigated in our previous work [1] and we shall concentrate on the isothermal case in the present investigation. As shown in Fig. 2, *Rc* decreases as the aspect ratio increases for both cases. As the aspect ratio is reduced, the convective motion is inhabited by the sidewalls. Therefore, a larger Rayleigh number is required to induce convection at a smaller aspect ratio. The case of isothermal sidewalls has higher *Rc* values than that of adiabatic sidewalls, especially for smaller values of the aspect ratio, since there is heat efflux through the sidewalls for the former case. It is also shown that the instability is incurred at lower *Rc* for Hopf bifurcation than for the exchange of stabilities. For the case of isothermal sidewalls (Fig. 2(b)), the curve for $(\epsilon, \lambda) = (0.2, 0.1)$ and that for $(\epsilon, \lambda = (0.6, 0.0075)$ merge at $d_x/d_y = 2.9$, which implies that the instability mode switches from Hopf bifurcation to exchange of stabilities at this aspect ratio when $(\epsilon, \lambda) = (0.2, 0.1)$. Namely, there is a tendency towards Hopf bifurcation at smaller aspect ratio. We may interpret this phenomenon as follows.

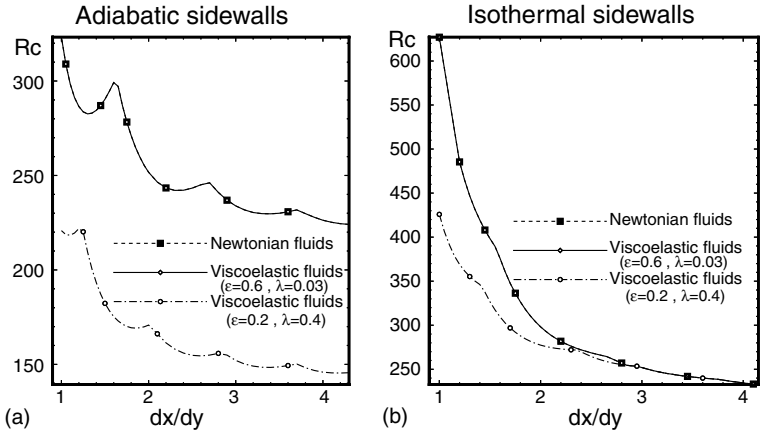


Fig. 2. Critical Rayleigh number versus aspect ratio for the case of adiabatic sidewalls (a) and isothermal sidewalls (b).

At a smaller aspect ratio, convection sets in at a higher Rayleigh number or at a more energetic state. The intensified energy state of the fluid triggers the elasticity of fluid, resulting in the oscillatory convection. Each curve in Fig. 2 consists of several piecewise continuous smooth curves, each smooth section of the curve corresponding to a particular mode number, i.e., number of convection cells at onset of instability. The mode number increases discretely as the aspect ratio $d_x/d_y$ increases. For example, the number of convection cells around $d_x/d_y = 2$ is two. It is interesting to note that $Rc$ decreases monotonically with respect to $d_x/d_y$ for the case of isothermal sidewalls, while $Rc$ increases for a short interval of $d_x/d_y$ before the number of cells increases and then $Rc$ drops again after the cell number increases for the case of adiabatic sidewalls. This difference is caused by the formation of small satellite convection cells near the sidewalls before the number of convection cells increases for the isothermal case. For example, the number of cells increases from one to two around $d_x/d_y \approx 1.65$ for the case of exchange of stabilities as shown in Fig. 2. For the adiabatic case, the $Rc$ increases for $1.3 \leqslant d_x/d_y \leqslant 1.65$ owing to the competition between one-cell mode and two-cell mode. On the other hand, small satellite cells begin to appear near the sidewalls for this range of aspect ratio in the isothermal case owing to the efflux of heat and, as a result, the $Rc$ does not increase before switching to the two-cell mode at $d_x/d_y \approx 1.65$. To visualize this, we show in Fig. 3 the convection patterns at various aspect ratios for the cases of adiabatic sidewalls and isothermal sidewalls at various aspect ratios when $(\epsilon, \lambda) = (0.6, 0.0075)$.

From now on, we consider the effects of domain irregularity on the convection. Only sidewall distortion is considered while keeping the top and bottom boundaries flat, which keeps $\partial T^s/\partial x$ identically zero and thus makes the basic state motionless. Fig. 4 shows the critical Rayleigh number and the boundary separating exchange of stabilities and Hopf bifurcation in the $\epsilon$–$\lambda$ plane for the irregular domain depicted in the same figure. Based on the results of Fig. 2, we easily expect that the critical Rayleigh number decreases for the domain with bulged sidewalls since it has a similar effect to the increased aspect ratio. Fig. 4 reveals that this domain has lower $Rc$ than the rectangular one as depicted in Fig. 1. Furthermore, the minimum Deborah number $\lambda_{\min}$ where the Hopf bifurcation occurs is raised to 0.082 from $\lambda_{\min} = 0.078$ of the case of rectangular domain (cf. Fig. 1). This is also consistent with the previous finding that there is a tendency towards Hopf bifurcation at smaller aspect ratio. Next, we consider another domain with sinusoidally distorted sidewalls, whose volume remains the same as that of the rectangular box of $d_x/d_y = 2.0$. Because the distorted sidewalls inhabit fluid motion, it is expected that this domain has a larger $Rc$ value than that of the rectangular domain. Fig. 5 shows the critical Rayleigh number and the boundary separating exchange of stabilities and Hopf bifurcation in the $\epsilon$–$\lambda$ plane for this domain. As expected the critical Rayleigh number is increased as compared to that of the rectangular domain depicted in Fig. 1. On the other hand, the minimum Deborah number that induces Hopf bifurcation, $\lambda_{\min}$, is lowered to about 0.076. Since the $Rc$ increases as $d_x/d_y$ decreases as shown in Fig. 1, the previous assertion that smaller aspect ratio tends to induce Hopf bifurcation may be rephrased as follows. If instability sets in at a higher Rayleigh number for a specific shape of the domain, the minimum Deborah number where Hopf bifurcation can be induced, $\lambda_{\min}$, takes a lower value. In the sequel, we investigate this assertion systematically employing various irregular domains. Fig. 6(a) shows the critical eigenfunction, $\Psi$, and critical

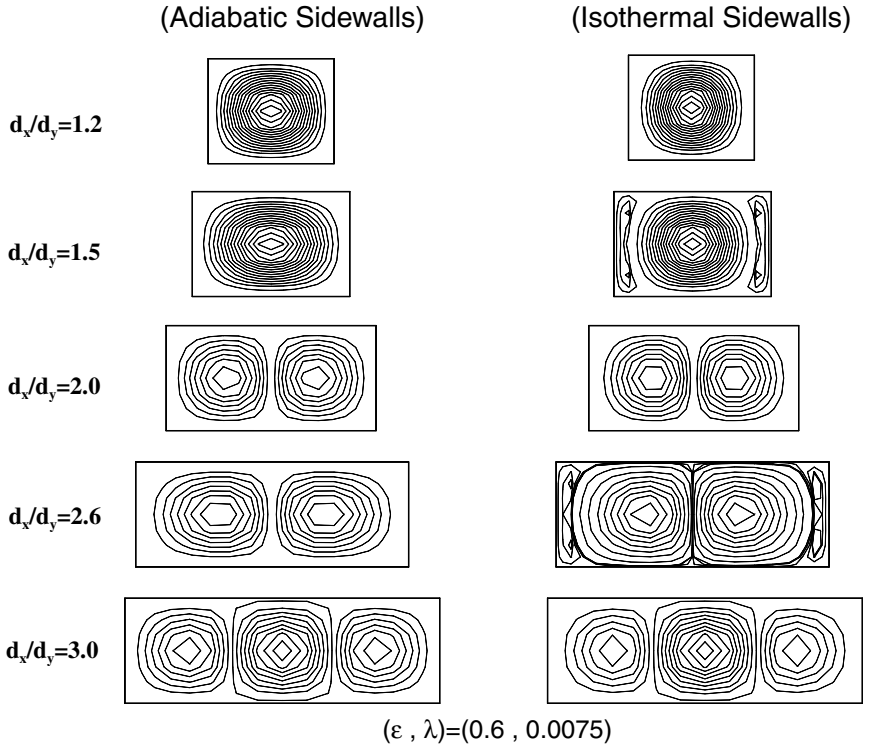


Fig. 3. Convection patterns at various aspect ratios for different thermal boundary conditions of the sidewalls.

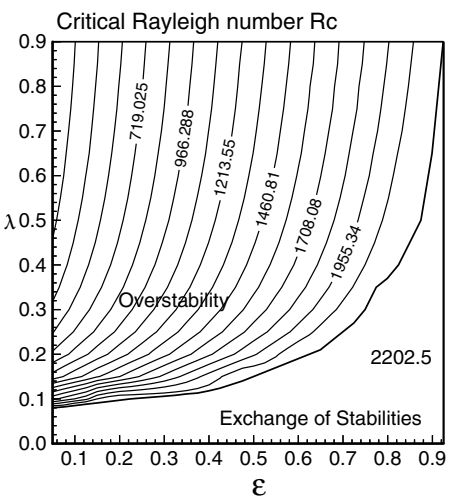


Fig. 4. The critical Rayleigh number and the boundary separating exchange of stabilities and Hopf bifurcation in the $\epsilon$–$\lambda$ plane for the irregular domain depicted in the figure.

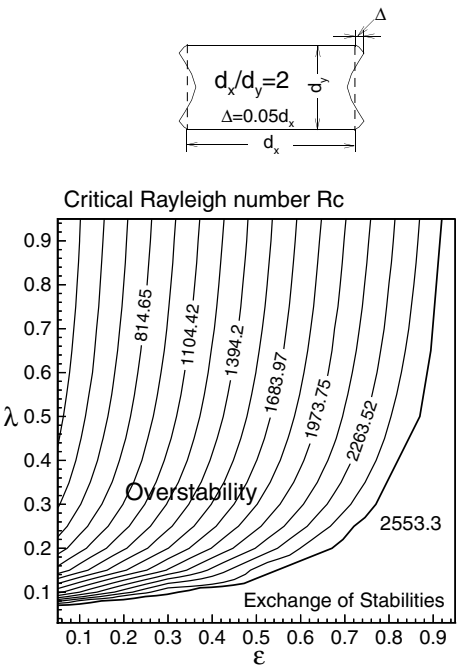


Fig. 5. The critical Rayleigh number and the boundary separating exchange of stabilities and Hopf bifurcation in the $\epsilon$–$\lambda$ plane for the irregular domain depicted in the figure.

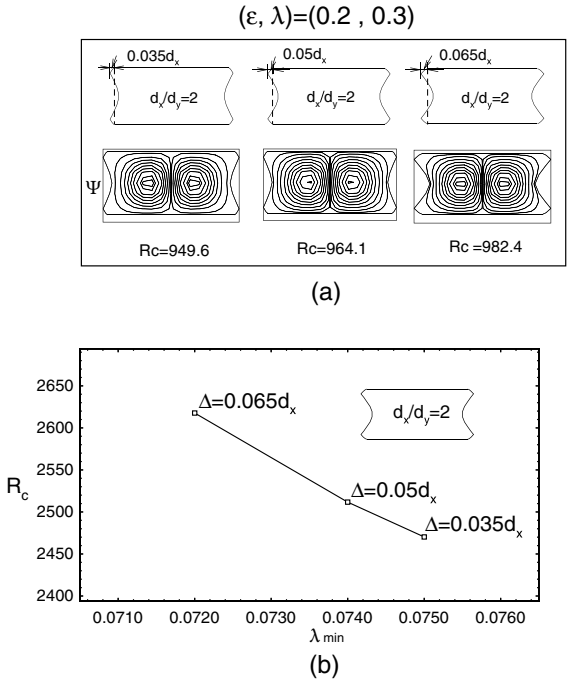


Fig. 6. (a) Critical eigenfunction ($\Psi$) and critical Rayleigh number for the shape of Fig. 5 when $(\epsilon, \lambda) = (0.2, 0.3)$ for the aspect ratio ($d_x/d_y = 2.0$) and (b) $Rc$ versus $\lambda_{\min}$ ($d_x/d_y = 2.0$).

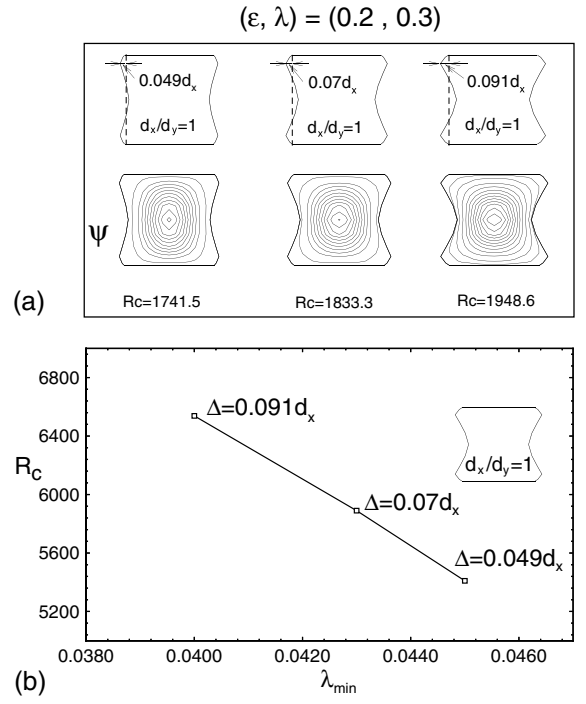


Fig. 7. (a) Critical $\Psi$ and $Rc$ when $(\epsilon, \lambda) = (0.2, 0.3)$ for $d_x/d_y = 1.0$. (b) $Rc$ versus $\lambda_{\min}$ ($d_x/d_y = 1.0$).

Rayleigh number for the shape of Fig. 5 when $(\epsilon, \lambda) = (0.2, 0.3)$ for various degree of distortion. These values of viscoelastic parameters correspond to the occurrence of Hopf bifurcation. It is shown that the $Rc$ increases as the distortion of the sidewalls becomes larger. Fig. 6(b) shows the relation between $\lambda_{\min}$, the minimum Deborah number where Hopf bifurcation is incurred for the domains under consideration, and the critical Rayleigh number $Rc$ at this value of Deborah number. As the distortion becomes larger, $Rc$ increases and $\lambda_{\min}$ decreases. This is consistent with the previous assertion that $\lambda_{\min}$ takes a lower value as the $Rc$, where the Hopf bifurcation sets in, takes a higher value. Fig. 7(a) and (b) plot similar results to those of Fig. 6(a) and (b) for the case of $d_x/d_y = 1.0$. Based on previous results, it is expected that overstability is also valid for $(\epsilon, \lambda) = (0.2, 0.3)$ and $d_x/d_y = 1.0$ since it is true for the larger aspect ratio of $d_x/d_y = 2.0$ (Fig. 6). This has been confirmed by solving the eigenvalue problem for these parameter values. The resulting velocity eigenfunctions $\Psi$ are shown in Fig. 7(a). The critical Rayleigh numbers for $d_x/d_y = 1.0$ are found to be higher than those for $d_x/d_y = 2.0$. As previously, $Rc$ increases with respect to the distortion ratio $\Delta$ for the present shape. Fig. 7(b) also reveals that $Rc$ increases and $\lambda_{\min}$ decreases as the distortion becomes larger. For completeness, we plot similar results for the case of $d_x/d_y = 0.5$ in Fig. 8(a) and (b).

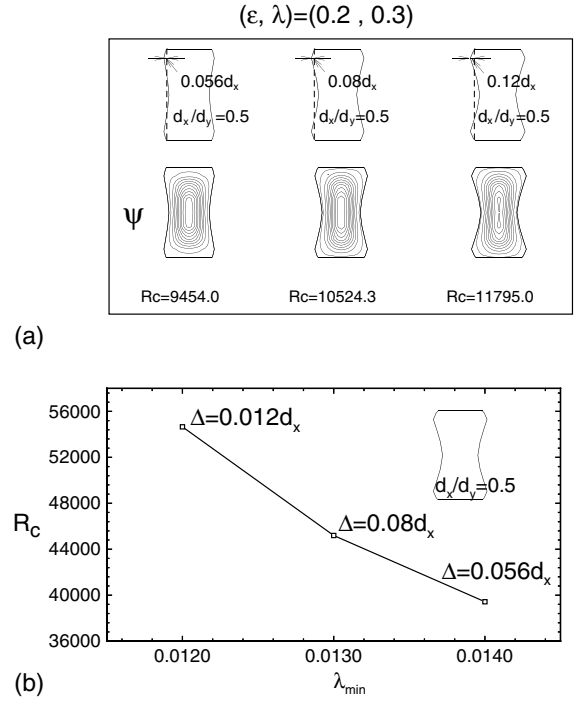


Fig. 8. (a) Critical $\Psi$ and $Rc$ when $(\epsilon, \lambda) = (0.2, 0.3)$ for $d_x/d_y = 0.5$. (b) $Rc$ versus $\lambda_{\min}$ ($d_x/d_y = 0.5$).

## 5. Conclusion

We have investigated the linear hydrodynamic stability problems of viscoelastic fluids in arbitrary finite domains. Special interest is to find a shape where the Hopf bifurcation occurs at a small Deborah number. It has been found that the geometric shape affects the onset of convection appreciably. Also investigated is the difference in the switching pattern of cell numbers as the aspect ratio varies, between the isothermal sidewalls and the adiabatic sidewalls.

In general, the critical Rayleigh number decreases as the aspect ratio increases or the domain's sidewall distorts in such a way that its virtual aspect ratio increases as in the case of Fig. 4. The sidewall distortion in Fig. 5 has the effect of decreased aspect ratio. It is found that smaller aspect ratio tends to induce Hopf bifurcation. It is also found that the minimum Deborah number where Hopf bifurcation can be induced takes a lower value if instability sets in at a higher Rayleigh number. The results of the present investigation may be exploited to design shapes of convection box where Hopf bifurcation occurs at realistic low values of Deborah number, which will enhance the usefulness of the natural convection system as a rheometry tool.

## Acknowledgements

This works was supported by grant No. R01-2003-000-10224-0 from Korea Science and Engineering Foundation.

## References

[1] H.M. Park, D.H. Ryu, Rayleigh–Bénard convection of viscoelastic fluids in finite domains, J. Non-Newtonian Fluid Mech. 98 (2001) 169–184.
[2] H.M. Park, D.H. Ryu, Nonlinear convective stability problems of viscoelastic fluids in finite domains, Rheol. Acta 41 (2002) 427–440.
[3] H.M. Park, D.H. Ryu, Hopf bifurcation in thermal convection of viscoelastic fluids within finite domains, J. Non-Newtonian Fluid Mech. 101 (2001) 1–19.
[4] R.G. Larson, Instabilities in viscoelastic flows, Rheol. Acta 31 (1992) 213–263.
[5] D. Haziavramidis, H.C. Ku, A pseudospectral method for the solution of the two-dimensional Navier–Stokes equations in the primitive variable formulation, J. Comput. Phys. 67 (1986) 361–371.
[6] J.F. Thompson, Z.U.A. Warsi, Numerical Grid Generation, North-Holland, The Netherlands, 1985.
[7] S. Chandrasekhar, Hydrodynamic and Hydromagnetic Stability, Oxford Univ. Press, London, 1961.